Received: 16 April 2020 | Revised: 18 June 2020 | Accepted: 26 June 2020

DOI: 10.1002/rra.3690

RESEARCH ARTICLE

WILEY

Assessing the potential for spectrally based remote sensing of salmon spawning locations

Lee R. Harrison[1,2] | Carl J. Legleiter[3] | Brandon T. Overstreet[4] | Tom W. Bell[2] | John Hannon[5]

[1]National Oceanic and Atmospheric Administration, Southwest Fisheries Science Center, Santa Cruz, California

[2]Earth Research Institute, University of California, Santa Barbara, California

[3]U.S. Geological Survey, Integrated Modeling and Prediction Division, Golden, Colorado

[4]U.S. Geological Survey, Oregon Water Science Center, Portland, Oregon

[5]United States Bureau of Reclamation, Sacramento, California

Correspondence
Lee R. Harrison, National Oceanic and Atmospheric Administration, Southwest Fisheries Science Center, Santa Cruz, CA 95060.
Email: lee.harrison@noaa.gov

Funding information
NOAA UAS Program Office, Grant/Award Number: Grant Number P1610802

Abstract

Remote sensing tools are increasingly used for quantitative mapping of fluvial habitats, yet few techniques exist for continuous sampling of aquatic organisms, such as spawning salmonids. This study assessed the potential for spectrally based remote sensing of salmon spawning locations (i.e., redds) using data acquired from unmanned aircraft systems (UAS) along a large, gravel-bed river. We developed a novel, semi-automated approach for detecting salmon redds by applying machine learning classification and object detection techniques to UAS-based imagery. We found that both true colour (RGB) and hyperspectral imagery could be used to identify salmon redds, though with varying degrees of accuracy. Redds were mapped with accuracies of ~0.75 from RGB imagery using logistic regression and support vector machines (SVM) classification algorithms, but this type of data could not be used to identify redds using Object-based Image Analysis (OBIA). The hyperspectral imagery was more useful for mapping salmon redds, with accuracies greater than 0.9 for both logistic regression and SVM classifiers; OBIA of the hyperspectral data resulted in redd detection accuracies up to 0.86. The hyperspectral imagery also yielded complementary physical habitat information including water depth and substrate composition, which we quantified on the basis of a spectrally based chlorophyll absorption ratio. Overall, the hyperspectral imagery more effectively identified salmon spawning locations than RGB images and was more conducive to the classification approaches we evaluated. Each type of remotely sensed data had advantages and limitations, which are important for potential users to understand when incorporating UAS-based data collection into river ecosystem studies.

KEYWORDS

hyperspectral, machine learning, redds, remote sensing, salmon, spawning, UAS

1 | INTRODUCTION

River ecosystems are structured by physical and biological processes operating over a range of spatial and temporal scales (Beechie et al., 2010). Characterizing variability in riverine landscapes, or riverscapes, is critical for understanding how organisms interact with habitat and for improving management and conservation of anadromous salmonids (Fausch, Torgersen, Baxter, & Li, 2002). Recent advances in fluvial remote sensing facilitate quantitative mapping of riverscapes and a number of new tools enable spatially continuous sampling of habitat throughout entire river systems (Carbonneau, Fonstad, Marcus, & Dugdale, 2012). For example, various remote

sensing methods have been developed to quantify the fundamental attributes of river corridors, as well as channel change, from reach to regional scales using satellite, airborne, or ground-based acquisitions (Piegay et al., 2020). These remote sensing tools provide a means of characterizing the physical habitat of rivers, which forms the basic template for salmonids during their freshwater life-stages. However, comparable remote sensing techniques for continuously sampling aquatic biota, such as spawning salmonids, are generally lacking.

Pacific salmon (*Oncorhynchus* spp.) have complex life histories and inhabit a range of riverine habitat types over the course of their lives. During spawning, salmon migrate to natal rivers in search of habitat suitable for reproduction. Female salmon typically select spawning sites where they can construct redds in areas with suitable water depth, velocity (Moir & Pasternack, 2008), substrate size (Riebe, Sklar, Overstreet, & Wooster, 2014), channel morphology (Hanrahan, 2007), and hyporheic flows (Geist & Dauble, 1998). Once a female salmon identifies a suitable spawning location, she uses her tail to dig a redd (i.e., nest) in gravel and deposits her eggs in the substrate. A completed redd consists of a pot, which is the upstream depression resulting from female digging, and a tailspill, which is where the excavated gravel is stored on the downstream end of the redd. The completed redds are often brighter and visually distinct from the undisturbed substrate.

The number of redds constructed in a river is an important indicator of overall spawner abundance and salmon redds are also a common metric used to evaluate river restoration performance. Redd counts can provide insight on how spawning salmon utilize available habitat across a riverscape, which can help inform species management efforts (Fausch et al., 2002). Spatially and temporally continuous redd sampling has been used to assess patterns in spawning activity and population trends at the river network scale (Isaak & Thurow, 2006). When detailed geospatial information on redd locations is available, redd mapping combined with hydraulic habitat modelling can be used to examine controls on salmon spawning preferences in natural (Benjankar, Tonina, Marzadri, McKean, & Isaak, 2016) and restored river reaches (Harrison et al., 2019). While the value of redd count data is widely recognized in salmon population assessments (Gallagher, Hahn, & Johnson, 2007), fine-scale spatial data on individual salmon spawning locations are often unavailable (Lapointe, 2012), thus creating a need for improved tools to effectively map salmon redds across a range of spatial scales.

Traditional redd mapping approaches involve manual surveys conducted by wading in shallow channels where flow conditions permit or by using boats on deeper river channels (Gallagher & Gallagher, 2005). On larger rivers, redds have been mapped from aerial imagery obtained from fixed-wing aircraft (Geist & Dauble, 1998) and through visual counts made by observers during helicopter flights (Isaak & Thurow, 2006). These conventional methods of redd mapping are subject to several important limitations, however. For example, ground surveys are time consuming and tend to be conducted over short spatial extents, providing limited spatial information on where salmon choose to spawn. Ground surveys are also dependent on river discharge and may not be feasible during high flows. Remote sensing techniques can help overcome these limitations by providing greater spatial coverage and higher resolution, essentially continuous information on river corridors (Tomsett & Leyland, 2019). However, remotely sensed imagery acquired from manned aircraft are expensive and require flight planning coordination with contractors, limiting the ability to rapidly collect imagery once salmon spawning begins. While a number of image-based techniques have been developed to map river corridors (Hugue, Lapointe, Eaton, & Lepoutre, 2016; Legleiter, Roberts, & Lawrence, 2009), remote sensing imagery commonly has pixels on the order 1–2 m^2, which may be too coarse to identify salmon redds, which have characteristic areal extents of roughly 10 m^2 (Bjornn & Reiser, 1991). Redd mapping via traditional fixed-wing aircraft and helicopters may also involve substantial human risk (Groves, Alcorn, Wiest, Maselko, & Connor, 2016). Furthermore, while manned aircraft provide broader spatial coverage, disparities might exist between visual redd counts made during manned aircraft flights and those derived from analysis of aerial imagery (Visser, Dauble, & Geist, 2002).

Unmanned aircraft systems (UAS) represent an appealing alternative to these traditional field methods and remote sensing approaches that potentially could be used to identify redds. For example, because UAS can be deployed from low altitudes and travel slowly or even hover, these platforms can acquire images with sufficiently high spatial resolution to identify small-scale features like isolated salmon redds. UAS have emerged as a means for characterizing river bathymetry in small rivers using Structure-from-Motion (SfM) photogrammetry techniques (Dietrich, 2017) and in larger river channels using Optimal Band Ratio Analysis (OBRA) (Legleiter & Harrison, 2019). UAS also have been used to effectively characterize fluvial habitats based on classification systems (Woodget, Visser, Maddock, & Carbonneau, 2016) or hydraulic habitat modelling (Tamminga, Hugenholtz, Eaton, & Lapointe, 2015). Groves et al. (2016) used video obtained from UAS to visually identify salmon redds along the Lower Snake River in Idaho, USA, and found that UAS-based redd counts were more accurate than redd counts obtained by observers onboard manned helicopter flights. Roncoroni and Lane (2019) developed a UAS-based technique to identify salmon redds using SfM-derived digital elevation models (DEMs) of difference and reported that their approach detected redds that were not captured by visual observations. Despite increased interest in UAS applications, these platforms remain an underutilized tool in salmon habitat studies (Harris, Nelson, Rieucau, & Broussard, 2019) and comparative evaluations of different UAS platforms, sensors, and image classification techniques are needed (Buters et al., 2019).

The goal of this study was to assess the potential for spectrally based remote sensing of salmon redds on a large, gravel-bed river. We developed a novel, semi-automated approach for detecting salmon redds by applying machine learning and object detection techniques to UAS-based imagery. We acquired true color (red, green, blue, or RGB) and hyperspectral imagery from small UAS and tested the redd mapping performance of two classification algorithms and an object detection technique. The performance of the various redd identification approaches was evaluated by comparing redd locations obtained from the imagery with salmon spawning locations

identified through ground surveys. All of the remotely sensed data and field measurements used in this study are available through a data release published by the U.S. Geological Survey (USGS) ScienceBase Catalog (Legleiter & Harrison, 2020).

2 | METHODS

2.1 | Study area

The American River is a tributary to the Sacramento River located in California's Central Valley (Figure 1) and has a total drainage area of 5,085 km^2. The lower American River supports two runs of Pacific salmon, including fall-run Chinook salmon (*Oncorhynchus tshawytscha*) and steelhead (*Oncorhynchus mykiss*; Moyle, Lusardi, Samuel, & Katz, 2017). Water discharge on the lower American River is regulated by Folsom and Nimbus Dams, which are located 48 and 37 km upstream from the confluence with the Sacramento River, respectively. The mean annual discharge measured 0.7 km downstream from Nimbus Dam at the U.S. Geological Survey (USGS) gage near Fair Oaks, CA (# 11446500) since dam closure in 1955 is 104 m^3/s. Regulation of the lower American has altered the natural flow regime by reducing winter and spring peak and pulse flows while increasing summer base flows (Beakes et al., 2014). Nimbus Dam is a passage barrier to upstream adult migration, preventing access to roughly 214 km of historically accessible habitat (Yoshiyama, Gerstung, Fisher, & Moyle, 2001). Salmon currently spawn in a ~30 km segment of the river downstream from Nimbus Dam.

Remotely sensed imagery obtained from manned aircraft have been used to map salmon redds on the American River for over 15 years. Historically, RGB imagery over a ~30 km river segment downstream from Nimbus Dam has been acquired two or three times each year during the fall-run Chinook spawning season (November to mid-December). Salmon redds are manually mapped from the imagery by visually identifying individual redds and these counts support system-wide estimates of the total redd abundance and distribution. Based on aerial redd counts from 2004 to 2016, the number of fall-run Chinook redds identified in the American River averaged roughly 3,000 per year (Hannon, 2017). In addition, redd counts are conducted in targeted reaches by wading, using jet

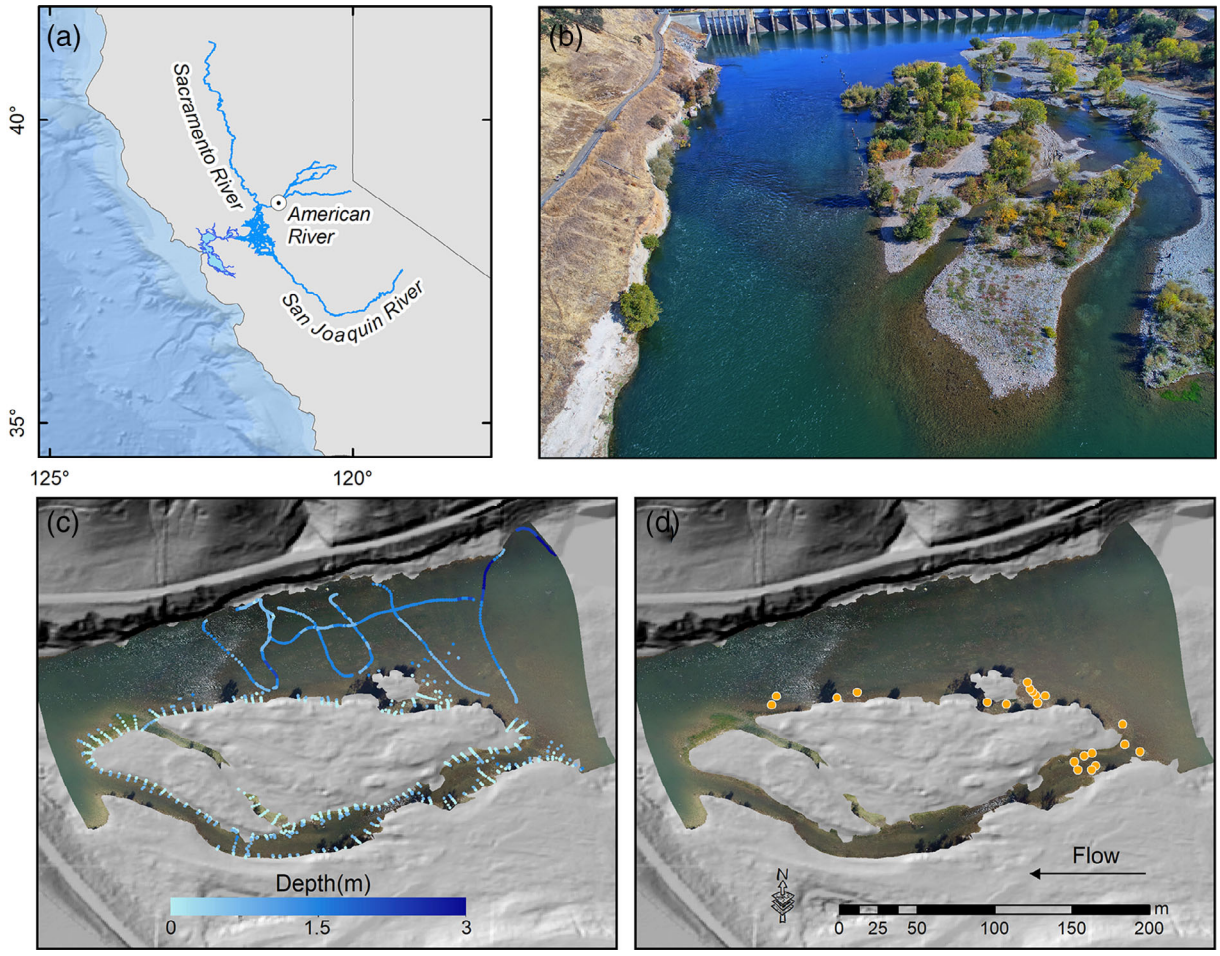

FIGURE 1 (a) Location of the American River in northern California, USA. (b) Oblique image of the study reach immediately downstream of Nimbus Dam. (c) RGB water-only image with field-based depth measurements overlain. Terrestrial areas are represented by a hillshade image produced from LiDAR topography. (d) Locations of salmon redds mapped in the field [Colour figure can be viewed at wileyonlinelibrary.com]

boats, or snorkeling; redd locations are surveyed using global positioning systems (GPS), where possible. While the overall approach provides an effective means of counting redds along the American (Zeug et al., 2014), the field surveys are time consuming and limited to short river reaches. Moreover, at times redd locations cannot be surveyed due to hazardous river conditions. Although aerial surveys provide a large-scale view of the river, manned flights are expensive and their utility for redd mapping depends on atmospheric conditions and river visibility at the time the images are acquired. Furthermore, disparities may exist between redd counts obtained from visual surveys compared to counts derived from analysis of aerial imagery (Visser et al., 2002). Ongoing efforts to monitor salmon population abundance and habitat enhancement project effectiveness on the American River rely on accurate redd counts, however, creating a compelling need to evaluate alternative approaches for remote sensing of salmon redds.

To gain insight regarding the potential for mapping salmon redds via UAS, we acquired remotely sensed data and field measurements along the lower American River. The study site was located immediately below Nimbus Dam (38.64°N, 121.22°W), in a reach referred to as Nimbus Basin, which has an upstream drainage area of 4,887 km^2. The Nimbus Basin study reach has a wide channel, minimal riparian vegetation, and clear water conditions, implying that the river might be characterized effectively via remote sensing. The study reach is an area of recent salmon habitat enhancement and gravel augmentation and features constructed mid-channel islands that divide the flow into a mainstem channel with pool-riffle morphology and a side channel connected to the adjacent floodplain (Figure 1b). The study reach was approximately 275 m long, had a mean wetted width of roughly 100 m, a mean depth of 0.98 m, and a water surface slope of 0.002 m/m at the time of image acquisition. The river bed sediment is composed of gravels and cobbles, which at the time of our surveys were coated with varying degrees of periphyton. All surveys were conducted during the fall-run Chinook salmon spawning season in November 2018 at a constant river discharge of 53.8 m^3/s.

2.2 | Field measurements

We mapped fall-run Chinook salmon redds using real-time kinematic (RTK) GPS receivers. Our surveys were conducted during the early stages of spawning activity observed on the American River in November 2018 and we mapped 21 newly constructed redds in areas that could be safely waded. While steelhead also spawn in the American River, their peak spawning activity occurs in January through April, thus they were not present during our spawning surveys. We identified fall-run Chinook salmon redd locations based on the distinctive pot/tailspill topography and the presence of disturbed sediment overturned by spawning fish. Redds that were under construction during our field campaign but were only partially completed were not included in our ground surveys.

Fall-run Chinook salmon tend to spawn in shallow water depths (0.2–0.8 m) but not in deeper pools (Moir & Pasternack, 2010). Therefore, in addition to using the imagery to detect salmon redds, we developed a water depth map (see Section 2.4) to identify shallow water and exclude areas that exceeded typical spawning depths. We measured water depths by using RTK GPS to survey the water surface elevation along the edge of the channel and bed elevations in areas of the river that could be safely waded; depths were estimated by subtracting each bed elevation from the nearest water surface elevation point. For the deeper parts of the channel we used a jet boat equipped with an acoustic Doppler current profiler (ADCP). The ADCP collected depth measurements at a sampling frequency of 1 Hz and the spatial position of each depth measurement was obtained from an integrated differential GPS receiver with a horizontal accuracy of approximately 0.15–0.2 m.

Completed salmon redds have an elliptical shape and often appear brighter than the surrounding, undisturbed substrate because the recently exposed bed surface within a redd lacks algae (Gallagher et al., 2007). To facilitate development of an image-based technique for identifying bright areas of the bed devoid of algae, we acquired ground-based reflectance data (i.e., field spectra) over 20 salmon redds and on 20 adjacent, undisturbed substrates. These data were collected using a FieldSpec HandHeld spectroradiometer (Analytical Spectral Devices, Inc., or ASD) that measured upwelling spectral radiance from 400 to 900 nm and was operated in reflectance mode via periodic measurements of a white reference panel. We analysed the field spectra to assess whether salmon redds had a unique spectral signature, relative to the undisturbed substrate, that could be identified in the hyperspectral imagery. Our analysis indicated that clean substrates lacking periphyton could be identified using a chlorophyll (*ch*) absorption ratio described further in Section 3.1. We chose to focus on mapped water depth and *ch* absorption ratios for detecting redds, as these predictors can help identify clean substrates located in shallow water. While water velocity, substrate size, and hyporheic flow also might be useful predictors of salmon redd locations, mapping these variables from the available imagery was beyond the scope of this investigation.

2.3 | UAS image acquisition and processing

We acquired UAS-based RGB and hyperspectral imagery and evaluated the potential utility of each data set for detecting redds. RGB imagery was acquired using a DJI Matrice 210 equipped with a Zenmuse X4S optical camera (DJI, 2020). The Matrice 210 is a four-rotor platform with a maximum payload capacity of 1.9 kg. We planned flight paths for the Matrice 210-Zenmuse UAS using DroneDeploy (DroneDeploy, 2020), with imagery collected along several parallel flight lines to ensure full coverage of the study reach. The Matrice 210-Zenmuse UAS was depolyed at a flying height of 75 m above ground level, with an average flight speed of 5 m/s. Raw Zenmuse images were georeferenced using RTK GPS and inertial motion unit (IMU) data recorded onboard the UAS and individual flight strips were combined into an orthorectified mosaic using Agisoft Metashape (Version 1.6.1; Agisoft, 2020). The resulting

TABLE 1 Summary of UAS data sets acquired on the American River, CA

Acquisition dates	Data type	Platform	Sensor	Height (m)	Pixel size (m)	Bands	Wavelengths (nm)
November 5–7, 2018	RGB	Matrice 210	Zenmuse X4S	75	0.15	3	480–660
November 5–7, 2018	Hyperspectral	Matrice 600	Nano-Hyperspec	119	0.15	252	398–956

orthoimage had a pixel size of 0.15 m (Table 1). The georeferenced RGB orthoimage was accurately co-registered with 19 surveyed ground control points (GCPs), with a root-mean-square error (RMSE) of 0.05 m.

The hyperspectral image was acquired using a DJI Matrice 600 with an integrated Nano-Hyperspec imaging system (Headwall Photonics, 2020a), which we refer to as the Nano. The larger Matrice 600 is a six-rotor platform with a maximum payload capacity of 6 kg. The Nano imagery acquired in this study had 252 spectral bands spanning the visible and near-infrared wavelength (λ) range from 398 to 956 nm. The Nano sensor is a pushbroom instrument that collects one row of cross-track spatial pixels per scan line as the platform moves forward during flight, with each pixel containing full spectral data. The Matrice 600-Nano UAS was depolyed at a flying height of 119 m above ground level, with an average flight speed of 1 m/s. The lower flight speed used for the Matrice 600-Nano UAS was designed to increase the image exposure time. We planned flight paths for the Matrice 600-Nano UAS using Universal Ground Control Software (UgCS, 2020). Hyperspectral imagery was obtained along parallel flight paths and raw flight strips were georeferenced using data from an onboard GPS and IMU and then combined into an orthoimage using Spectral-View version 5.5.1 (Headwall Photonics, 2020b) We applied calibration coefficients provided by Headwall, the Nano manufacturer, to convert digital numbers to radiance and then used a calibration tarp placed on the ground as an in-scene white reference to produce a final reflectance image. The initial hyperspectral orthoimage had poor alignment with field-surveyed GCPs and additional georeferencing was required to improve horizontal accuracy. We used ENVI software tools to perform image to image registration with the RGB orthoimage as the base. This process greatly improved coregistration between the images comprising the mosaic and with our field-surveyed GCPs. The final hyperspectral orthoimage had a RMSE of 0.77 m, relative to our surveyed GCPs.

2.4 | Water depth retrieval

To assist in identifying shallow regions of the channel conducive to redd building, we mapped water depth using the Optimal Band Ratio Analysis (OBRA) framework established through previous research on similar rivers (Legleiter et al., 2009; Legleiter & Harrison, 2019). Only a brief overview of OBRA is provided here and greater detail can be found in the original publications. Depths were estimated from the image data based on relationships between depth d and reflectance $R(\lambda)$ expressed in terms of the image-derived quantity

$$X = \ln\left[\frac{R(\lambda_1)}{R(\lambda_2)}\right], \quad (1)$$

where $R(\lambda_1)$ and $R(\lambda_2)$ are reflectances in the pair of wavelengths selected via OBRA, which regresses field measurements of d versus X values for all possible band combinations. The optimal band ratio is that which yields the highest regression R^2. In this study, we included an X^2 term in the regression against d to improve depth retrieval in the deeper water (Legleiter & Overstreet, 2012).

2.5 | Image classification

As an alternative to visually identifying salmon redds from the UAS imagery, we sought to develop and test a semi-automated workflow that would be repeatable and less subjective than current redd detection methods (Figure 2). To pursue this objective, we developed 10 raster stacks, which included a combination of the original image bands and depth and *ch* ratio predictors derived from the images. For the RGB imagery, we used two sets of redd location predictors: the raw RGB data and the RGB image bands combined with a water depth map produced via OBRA. For the hyperspectral imagery, we evaluated three sets of image-based predictors. First, we used eight spectral bands resampled from the original hyperspectral data to match the visible and near-infrared (425–910 nm) bands of the WorldView-3 (WV3) satellite. We used a subset of the full 252 available spectral bands to reduce computational time during the redd classification procedure. The second set of hyperspectral predictors included the eight WV3 bands plus a depth map derived via OBRA of the same eight bands. The third set of hyperspectral predictors included the eight WV3 spectral bands, depth derived via OBRA of the original 252-band hyperspectral image, and *ch* absorption ratio values.

We paired field-surveyed redd locations with the raster stacks derived from the RGB and hyperspectral imagery to develop image-based redd classifications. We developed a training data set by manually digitizing points within the perimeter of each field-mapped redd (n = 300) and generated an equivalent number of random points from other areas in the images that were not used for spawning. We extracted pixel values for redd and non-redd locations from each raster stack and used them as input to two binary classification techniques: logistic regression and support vector machines (SVMs). We randomly selected 25% of the training data to use for model validation, developed classification models using the remaining 75% of the data and evaluated the performance of each classifier using the withheld validation data. The classifiers were used to develop redd probability maps in which each pixel in the image was assigned a probability

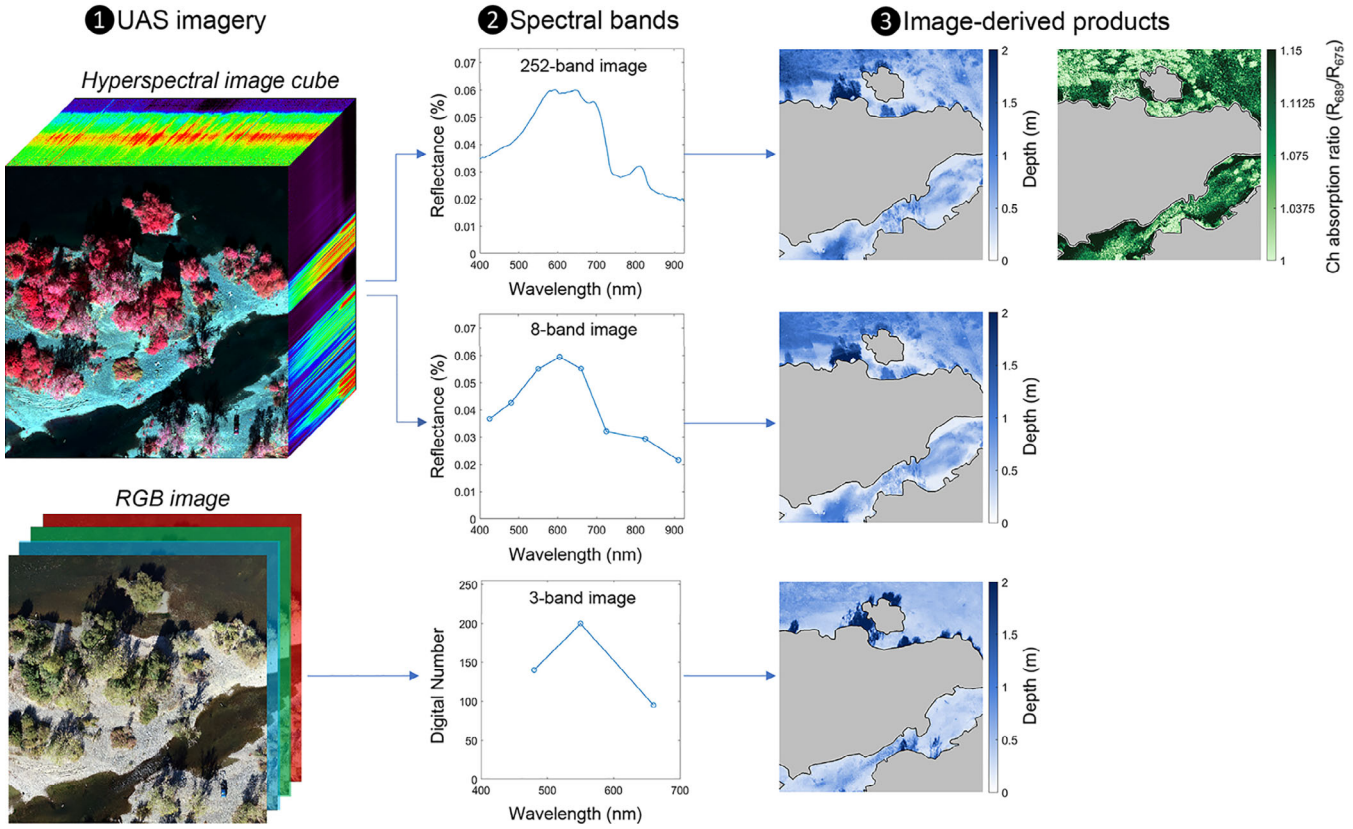

FIGURE 2 Schematic representation of the overall redd mapping workflow developed in this study, which includes: (1) acquiring UAS-based hyperspectral image data (shown as a false-colour composite) and RGB imagery; (2) resampling the hyperspectral image data from 252 to eight spectral bands; and (3) producing a map of the chlorophyll (*ch*) absorption ratio from the 252-band hyperspectral image and maps of water depth from the 252-, 8-, and 3-band images. These image-derived products were then used to classify redds using machine learning techniques [Colour figure can be viewed at wileyonlinelibrary.com]

of containing a redd, with probabilities ranging from zero to one. We examined the quality of predictions made by the two classifiers on the validation data by computing classification accuracy, precision, and recall. Accuracy can be interpreted as the proportion of correct predictions made by the classifier, precision is the ability of a classifier not to misclassify a negative sample (non-redd) as positive (redd), and recall is the ability of the classifier to identify all of the positive samples.

We used the redd probability maps derived from the two classifiers to test a semi-automated, Object-based Image Analysis (OBIA) approach to detect redds using the ENVI feature extraction tool (Harris Geospatial, 2008). OBIA involves image segmentation, segment classification, and generalization based on spectral, spatial, and textural characteristics. We used OBIA to segment redd probability maps into regions of pixels, computed attributes for each region to create objects, and then classified the objects with a nearest neighbour classifier to represent the boundaries of individual redds as vector polygons. The potential advantage of incorporating OBIA into the redd mapping workflow was that it provided vector polygons for each individual redd, thereby obviating the need to manually decide whether a given cluster of image pixels was a redd. Although OBIA could have been applied to the raw imagery, this approach would have required developing rules for each image data set, whereas using the redd probability maps allowed us to conduct OBIA using a single input raster. We performed a sensitivity analysis of OBIA predictions by varying the redd probability threshold between 0.1 and 0.9 in 0.1 increments and calculating the accuracy, precision, and recall for each threshold.

3 | RESULTS

3.1 | Quantifying water depth and substrate optical properties

This study examined the potential for spectrally based remote sensing to identify salmon redds. To achieve this objective, we acquired UAS-based RGB and hyperspectral imagery, measured water depths and field spectra, and used the field data to develop maps of water depth and a chlorophyll (*ch*) absorption ratio for use as image-based predictors of redd occurrence. Results from the depth retrieval analysis for the RGB, 8-band, and 252-band images are summarized in Figure 3.

For the RGB imagery, quadratic OBRA did not result in accurate depth retrieval (Figure 3a,d). Defining X using 660 and 480 nm as the numerator and denominator, respectively, resulted in an R^2 of 0.45

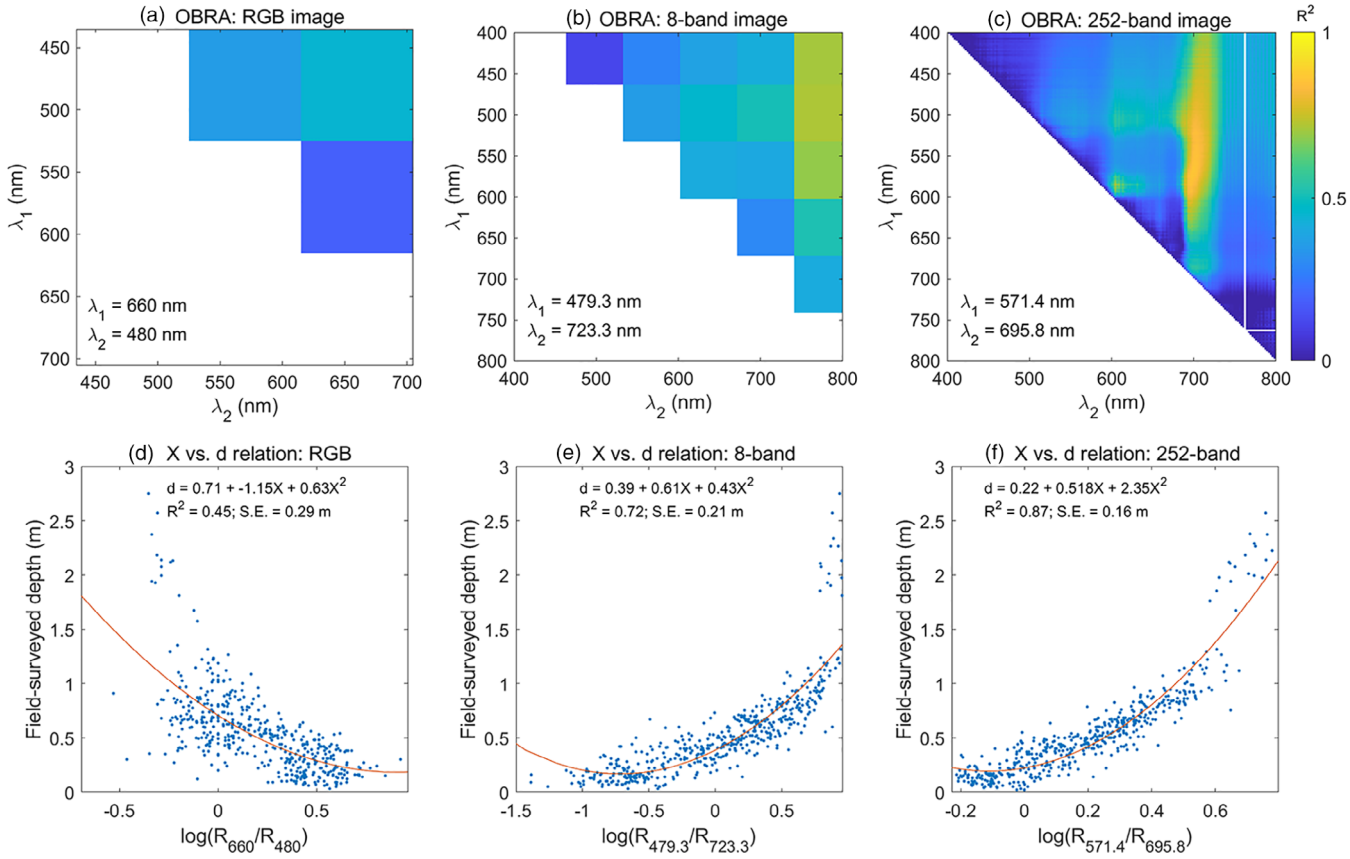

FIGURE 3 OBRA output for (a) RGB, (b) 8-band and (c) 252-band images. The corresponding *X* versus *d* relationships for each type of image are shown in (d-f) [Colour figure can be viewed at wileyonlinelibrary.com]

and standard error of 0.29 m (Figure 3a,d) for the *X* versus *d* calibration relationship. The depth map produced from the RGB imagery tended to homogenize predicted depths, without capturing the spatial variation between shallow and deep regions of the river. We concluded that the RGB sensor used in this study did not provide useful depth information and we did not include water depth maps derived from the RGB imagery as predictors in subsequent redd classification analyses.

OBRA of the Nano data spectrally resampled to the eight WV3 bands yielded more accurate depth retrieval. Defining *X* using 480 and 723 nm in the numerator and denominator, respectively, resulted in an R^2 of 0.72 and a standard error of 0.21 m in the *X* versus *d* calibration relation (Figure 3b,e). Depth estimates were generally accurate for depths between 0.25 and 1.4 m, but depths tended to be over-predicted in shallow areas and under-predicted in deeper pools due to the use of a quadratic *X* versus *d* relation (Figure 3e).

The most accurate depth estimates were obtained using the full 252-band hyperspectral image. Defining *X* using 571 and 696 nm in the numerator and denominator, respectively, yielded an R^2 of 0.87 and a standard error of 0.16 m for the *X* versus *d* calibration relation (Figure 3c,f). The OBRA matrix shown in Figure 3c indicated that in addition to the optimal band ratio, several other wavelength combinations would have produced an *X* versus *d* relation nearly as strong. Moreover, the *X* versus *d* relation developed using the full 252-band image (Figure 3f) did not lead to the same biases of over-predicting shallow depths and under-predicting deeper depths that resulted from OBRA of the resampled eight-band Nano image (Figure 3e). Depth maps for both the original and resampled Nano data sets effectively captured spatial variations in water depth and were included as predictor variables in redd classification analyses.

Figure 4a shows the difference in brightness between the buried and exposed surfaces of a gravel particle that has been flipped on its side, as occurs when a female salmon disturbs the bed during redd construction. This photograph illustrates how the exposed surface is covered with periphyton whereas the buried surface lacks periphyton prior to disturbance, resulting in a pronounced difference in brightness between the two faces of the particle. Figure 4b provides an example of field spectra measured over the redd pot and tailspill, as well as over an adjacent undisturbed substrate. These field spectra captured a strong absorption feature (i.e., drop in reflectance) at a wavelength of 675 nm for the undisturbed substrate due to the presence of chlorophyll (*ch*). Similar *ch* absorption features at 675 nm were evident in field spectra collected from periphyton-covered substrates in an experimental outdoor stream channel (Legleiter & Overstreet, 2014). The same decrease in reflectance at 675 nm was not present in the field spectra from the salmon redd, however, because some of the gravel on the bed had been overturned to expose fresh surfaces that lacked periphyton (Figure 4b).

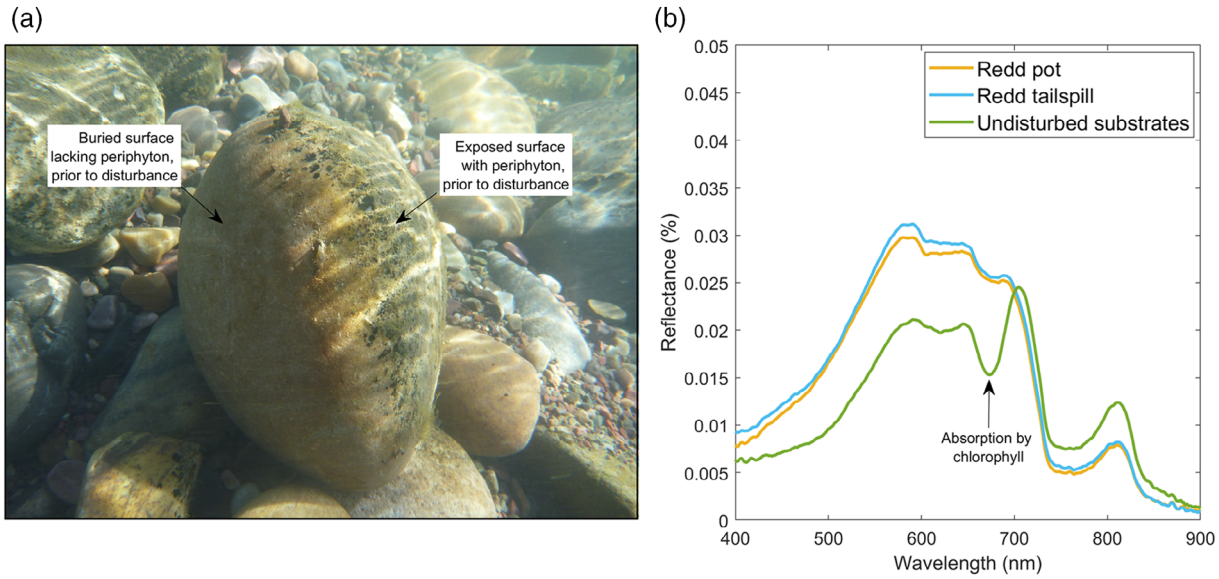

FIGURE 4 (a) Photograph of submerged gravel particle, illustrating the clean, buried surface, which lacks periphyton prior to disturbance by redd building versus the exposed surface, which contains periphyton prior to disturbance. (b) Field spectra collected over redd pot, tail and undisturbed substrates. Note the absorption by chlorophyll (*ch*) on the undisturbed substrates due to the presence of perihyton, which is not present in the redd spectra [Colour figure can be viewed at wileyonlinelibrary.com]

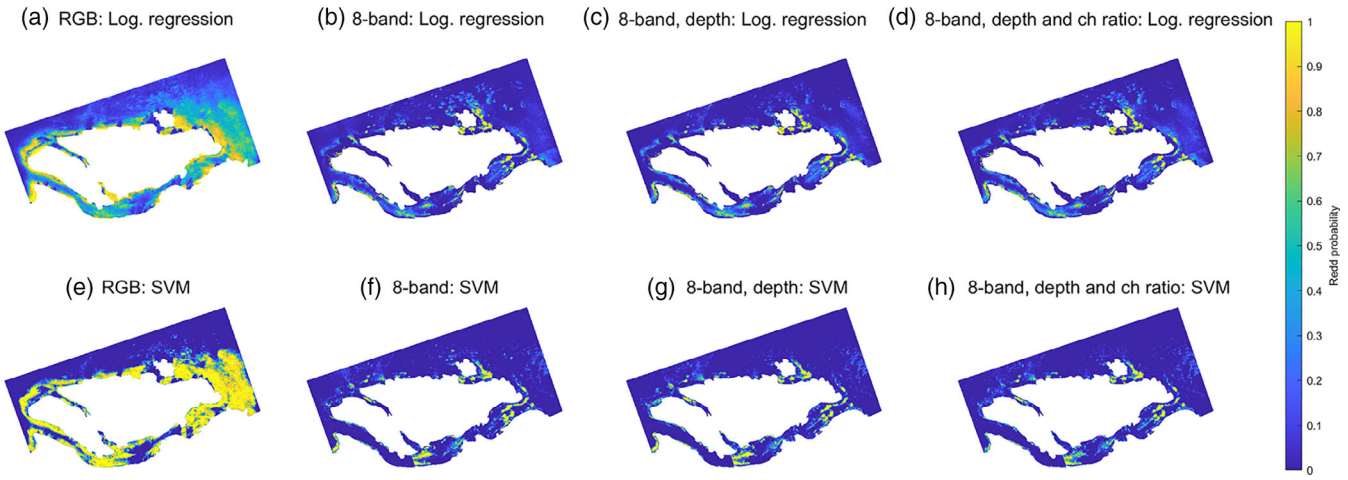

FIGURE 5 Predicted redd probabilities using logistic regression (top) and SVM (bottom) classification algorithms. A scale bar is provided in Figure 1 for reference [Colour figure can be viewed at wileyonlinelibrary.com]

To quantify and exploit this difference in measured reflectance between redd and non-redd areas, we defined a *ch* absorption ratio as *R*(689)/*R*(675) and used this simple index as a predictor for identifying salmon redds from the hyperspectral imagery. These *ch* ratio maps indicated that redds tended to have a *ch* ratio roughly equal to 1 and non-redd areas colonized by periphyton had *ch* ratios greater than 1. Examples of individual redds can be seen in the *ch* ratio map as white ellipses (Figure 2); these areas generally coincided with our field-surveyed redd locations.

3.2 | Spectrally based redd classification

Redd classifications derived using eight different candidate models are shown in Figure 5 and a summary of the accuracy, precision, and recall of each model is provided in Table 2. Redd probabilities for individual (0.15 m) pixels are shown in each panel of Figure 5, where cool colours represent a low predicted redd probability and warm pixels represent a high predicted redd probability. For the RGB imagery, both logistic regression and SVM classifiers predicted moderate to

TABLE 2 Comparison of redd classification performance using logistic regression and SVM classifiers

Model	Platform	Sensor	Candidate model	Classifier	Accuracy	Precision	Recall
1	M210	Zenmuse X4S	RGB bands	Logistic regression	0.76	0.73	0.77
2	M600	Nano-Hyperspec	8-band	Logistic regression	0.98	0.96	1.00
3	M600	Nano-Hyperspec	8-band, depth	Logistic regression	0.95	0.97	0.94
4	M600	Nano-Hyperspec	8-band, depth, *ch* ratio	Logistic regression	0.95	0.96	0.94
5	M210	Zenmuse X4S	RGB bands	SVM	0.76	0.83	0.73
6	M600	Nano-Hyperspec	8-band	SVM	0.95	1.00	0.91
7	M600	Nano-Hyperspec	8-band, depth	SVM	0.97	0.97	0.97
8	M600	Nano-Hyperspec	8-band, depth, *ch* ratio	SVM	0.97	0.99	0.95

high redd probabilities in the shallow channel margins, with few if any redds predicted in the main channel along the northern portion of the project reach. Areas with predicted redds occurred as large, continuous zones, but few isolated redds on the scale of the field-surveyed redds, which were on the order of ~10 m^2, were predicted (Figure 5a, e). The RGB-based redd predictions had accuracies of 0.76 for both logistic regression and SVM classifiers, respectively (Table 2). Both classifiers had high precision, indicating that non-redd areas were generally classified correctly. Recall values for the RGB data sets were 0.77 and 0.73 for the two classifiers, indicating a tendency to misclassify a portion of redds as non-redds.

Relative to the RGB imagery, the Nano hyperspectral image generally yielded more reliable predictions of where spawning salmon constructed redds. In particular, classifications based on the Nano imagery more effectively predicted isolated clusters of pixels with high redd probabilities, in contrast to the large swaths of high redd probability predicted from the RGB imagery. These patterns were in agreement with our field-mapped redds, which consisted of isolated circular or elliptical redds. Accuracies for each of the six candidate hyperspectral models were high for both the SVM and logistic regression classifiers. In general, the precision was greater than or equal to the accuracy and recall, indicating that non-redd areas were rarely classified as redds (Table 2). In several instances, true redds were omitted from the classification, which reduced the accuracy and recall values. Nevertheless, all accuracy, precision, and recall values for the Nano imagery exceeded 0.9, indicating that both logistic regression and SVM machine learning techniques effectively classified redds.

3.3 | Object-based redd identification

Using the redd probability maps (Figure 5) as input, we used OBIA to delineate individual redds for each of the eight candidate models listed in Table 2. The OBIA approach did not effectively define individual redds from the RGB redd probability maps. We attributed this result to the tendency for both logistic regression and SVM classifiers to over-predict the areal extent of potential redds (Figure 5a,e) rather than identifying smaller-scale features with more realistic areal extents of ~10 m^2.

Examples of the OBIA-derived redd polygons for Models 6–8 are shown in Figure 6 for an area located at the head of the side channel where six redds were mapped in the field. Model 6, which used redd probabilities derived from the eight-band image, identified the general perimeters of the six field-mapped redds, though the polygons were merged into three large polygons due to poor edge detection between redds (Figure 6a). Model 7, which included eight-band imagery and depth (Figure 6b), and Model 8, which included eight-band imagery, depth and *ch* ratio (Figure 6c), identified all six of the field-mapped redds, with clearer distinctions between individual predicted redds and the corresponding OBIA polygons.

A summary of the OBIA redd predictions derived from the Nano data using Models 2–4 and 6–8 is provided in Figure 7. We evaluated the sensitivity of OBIA predictions to the input redd probability used, by varying the threshold between 0.1 and 0.9 in 0.1 increments, and found that consistently accurate OBIA results were obtained using a threshold value equal to 0.8. For illustration, OBIA results obtained using a redd probability threshold value of 0.8 is shown in Figure 7.

The logistic regression-based redd predictions had accuracies between 0.61 and 0.75 and correctly identified between 81 and 86% of field-surveyed redds. Incorrect OBIA redd predictions occurred in several non-redd locations containing shallow water and patches of clean gravel, with the greatest number of incorrectly predicted redds obtained using the eight-band image (Figure 7a). The logistic regression model developed using the eight-band image, depth and *ch* ratio as input provided the best overall OBIA results of the three logistic models evaluated in this study (Figure 7c).

The SVM-based redd predictions had accuracies between 0.65 and 0.86 and correctly identified between 81 and 86% of the field-mapped redds, with the full model providing the best overall results (Figure 7f). OBIA redd predictions made using the SVM models as input had fewer misclassified redds than the logistic regression models. The full model including eight-band imagery, depth, and *ch* ratio values, combined with the SVM classifier did not have any misclassified redds, although it did omit three redds located on the northwestern margin of the mid-channel island (Figure 7f). These three redds were omitted by all six models and were smaller in areal extent and darker than the other field-mapped redds, suggesting that they may have been partially completed redds during the time of our field surveys. Of the six models evaluated, the full SVM model provided the best overall results (Figure 7f), with an accuracy of 0.86.

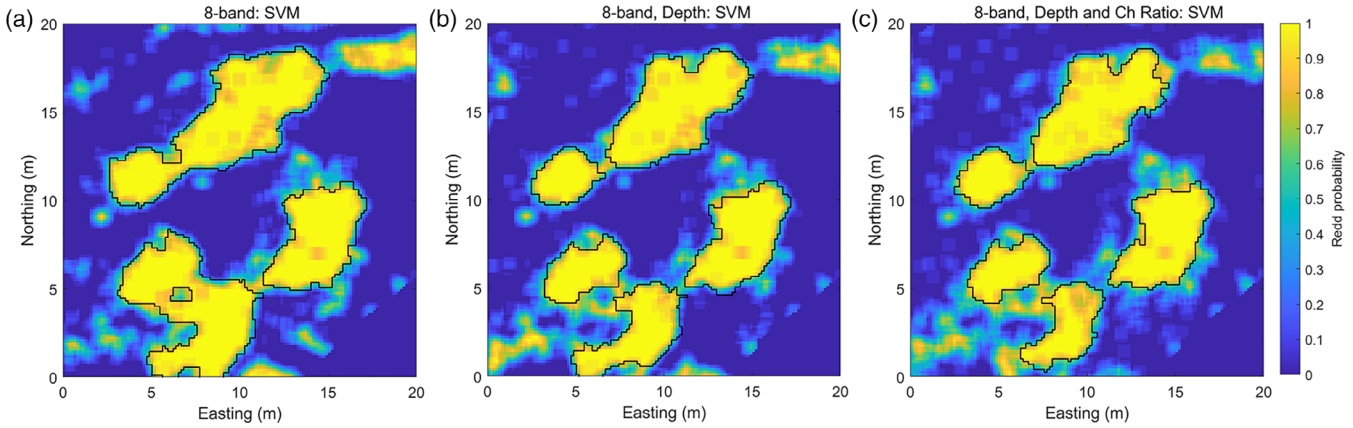

FIGURE 6 Example OBIA-derived redd polygons (black lines) overlain on redd probability maps for models (a) 6, (b) 7, and (c) 8 [Colour figure can be viewed at wileyonlinelibrary.com]

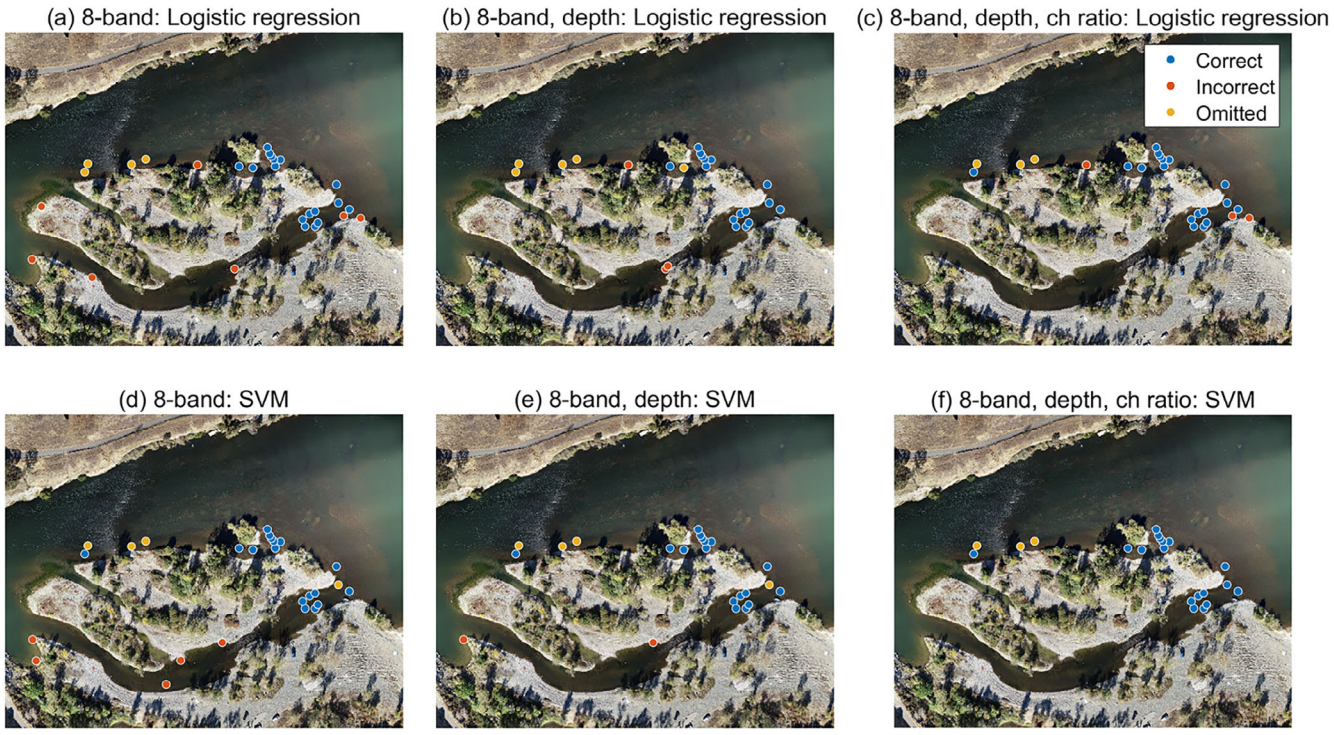

FIGURE 7 Predicted OBIA redd locations using eight spectral bands (a, d), eight spectral bands with depth (b, d) and eight spectral bands, depth, and chlorophyll (ch) absorption ratio (c, f), combined with logistic regression (top) and support vector machine learning (SVM) redd probability maps (bottom). In each plot, blue points represent correctly predicted redd locations, dark orange points represent incorrect redd predictions and light orange points represent locations where redds were mapped in the field but omitted by the OBIA. A scale bar is provided in Figure 1 for reference [Colour figure can be viewed at wileyonlinelibrary.com]

4 | DISCUSSION

4.1 | Advantages and limitations of spectrally based redd mapping

Understanding where adult salmon choose to spawn is essential for improving management and recovery of endangered salmon (Malcolm, Gibbins, Soulsby, Tetzlaff, & Moir, 2012). Given the limitations of traditional field-based approaches for redd mapping, a compelling need exists to develop remote sensing methods that are capable of detecting salmon redds and can be integrated with other geospatial data sets that describe physical habitat conditions. In this study we developed a semi-automated workflow for identifying redds using remotely sensed data acquired from small UAS. We used UAS-based RGB and hyperspectral imagery, ground surveyed redd locations, and measured water depths and field spectra to test redd classification approaches along a large,

clear-flowing river. We then used OBIA to map the perimeter of individual redds in classified images. While previous studies have mapped redds using UAS (Groves et al., 2016; Roncoroni & Lane, 2019), this is the first investigation to assess different sensors and multiple semi-automated classification techniques. Our redd mapping approach has the advantage of being based on a single image, rather than requiring two separate image acquisitions to produce a single map of redd locations (Roncoroni & Lane, 2019). In this study, the redd mapping methods we developed were applied to a single point in time, but the same approach also could be used with multiple images in a time series to examine spatial and temporal changes in redd abundance throughout the spawning season. Furthermore, this study demonstrated the potential for UAS-based redd mapping on a relatively large river, whereas previous studies on riverine habitat mapping via UAS have been conducted on smaller, shallow river channels (Dietrich, 2017; Roncoroni & Lane, 2019; Tamminga et al., 2015). The redd mapping approach developed here could be combined with other remote sensing data sets characterizing physical habitat variables (e.g., grain size, water depth, velocity, and temperature) across riverscapes to examine how salmon use existing habitats and to test hypotheses on redd site selection.

The redd mapping technique described herein represents an improvement over traditional redd mapping methods, as our approach offers a continuous view of the river with near-hyperspatial (0.1 m or smaller) pixel resolution. Image-based approaches provide a means of rapidly surveying a given reach and obtaining precise redd locations even in areas of the river that are too deep or swift to wade safely (Abt, Wittier, Taylor, & Love, 1989). Remotely acquired imagery also allows redds to be delineated without any direct physical contact, which is advantageous for mapping sensitive locations, such as salmon spawning sites. The fine resolution provided by the UAS imagery enabled detection of small-scale features that might be missed by other types of commonly used remote sensing data. For example, multispectral satellite data have been used to successfully map water depths on large rivers (Hugue et al., 2016; Legleiter & Harrison, 2019), but the lower spatial resolution typical of sensors like WorldView-3 (∼2 m) would likely be too coarse to identify individual redds. Multispectral or hyperspectral imagery obtained from manned aircraft could be acquired with smaller pixel sizes (∼0.5 m) and could facilitate increasing the spatial extent of redd mapping in future applications.

Our study demonstrated the utility of a semi-automated mapping approach that represents an improvement over previous methods, which rely on visual interpretation of remotely sensed imagery (Geist & Dauble, 1998; Groves et al., 2016). The most accurate classifications were produced from the hyperspectral imagery, while the RGB imagery evaluated in this study was not conducive to semi-automated classification. The inability of the RGB sensor to detect redds using logistic regression or SVM classifiers was somewhat surprising because redds could often be seen visually in the RGB images as areas substantially brighter than surrounding undisturbed substrates. The poor redd detection performance might be due to the low spectral resolution of the RGB sensor, which also might have limited the utility of these data for OBRA-based depth mapping. The hyperspectral sensor provided highly accurate predictions of redd locations, with accuracies greater than 0.9 for both logistic regression and SVM classifiers (Table 2), even when using a small, resampled eight-band subset of the 252 spectral bands available. Redd detection accuracies were greatest using the spectral bands in combination with derived water depth and *ch* ratio rasters as predictors.

We found that the full model, combined with the SVM classifier, provided the best results for OBIA-based redd delineation and a summary of this workflow is shown in Figure 8. Identifying redds based on visual interpretation of imagery alone (Figure 8a) may be challenging and redd detection was improved through the addition of water depth (Figure 8b), *ch* ratio (Figure 8c), and redd probability maps (Figure 8d). The water depth maps were able to identify redds to some degree, as depicted in the zoom panel of Figure 8b, where redds can be seen as deeper depressions relative to the surrounding shallow water. We found that the redd probability map closely reflected the *ch* ratio values at mapped redds, as shown in the zoom plots of Figure 8c,d. The *ch* ratio maps also identified a number of redds that were in the process of being constructed in the main channel (Figure 8c), though had not been completed during our field surveys.

The main strength of the OBIA approach was in detecting salmon redds with a high degree of confidence. The OBIA redd polygons were useful for filtering out small (less than 2 m^2) isolated clusters of non-redd image pixels, which improved overall classification performance. OBIA-based redd predictions were sensitive to the redd probability threshold used, with higher threshold probabilities resulting in improved accuracy metrics. However, using higher threshold probabilities also resulted in smaller predicted redd polygon areas. These results suggest that using a higher threshold probability (∼0.8) would result in improved accuracy for estimating the total number of redds in a given reach, whereas using a lower redd probability (∼0.5) would likely produce improved estimates of the area of individual redds. During our field surveys, we observed fish actively spawning on many of the redds we identified. For this reason, we did not survey detailed redd perimeters and thus do not have the data required to evaluate the potential for using OBIA to derive redd areas.

Despite being less useful for semi-automated redd classification, the RGB imagery still played a valuable role in the overall redd mapping workflow. The RGB imagery required roughly an order of magnitude less post-processing time, had better horizontal accuracies, and served as a base map for geo-referencing the Nano orthoimage. Given the ease of collecting and post-processing the RGB imagery, this type of data might be more suitable for generating a time series of daily or weekly redd counts throughout the spawning season, despite the potential shortcomings of using the imagery in the semi-automated workflow tested here. Using a combination of RGB imagery and hyperspectral imagery, in conjunction with the machine learning workflow developed in this study, would provide an effective means for salmon redd mapping in future applications. Our study also demonstrated the redd mapping potential provided by eight spectral bands, which we resampled from the original 252-band hyperspectral imagery. In future applications, a more cost-effective alternative could be to use a multispectral sensor deployable from a UAS. Data from such an instrument could potentially be used to identify redds using the general workflow developed in this study.

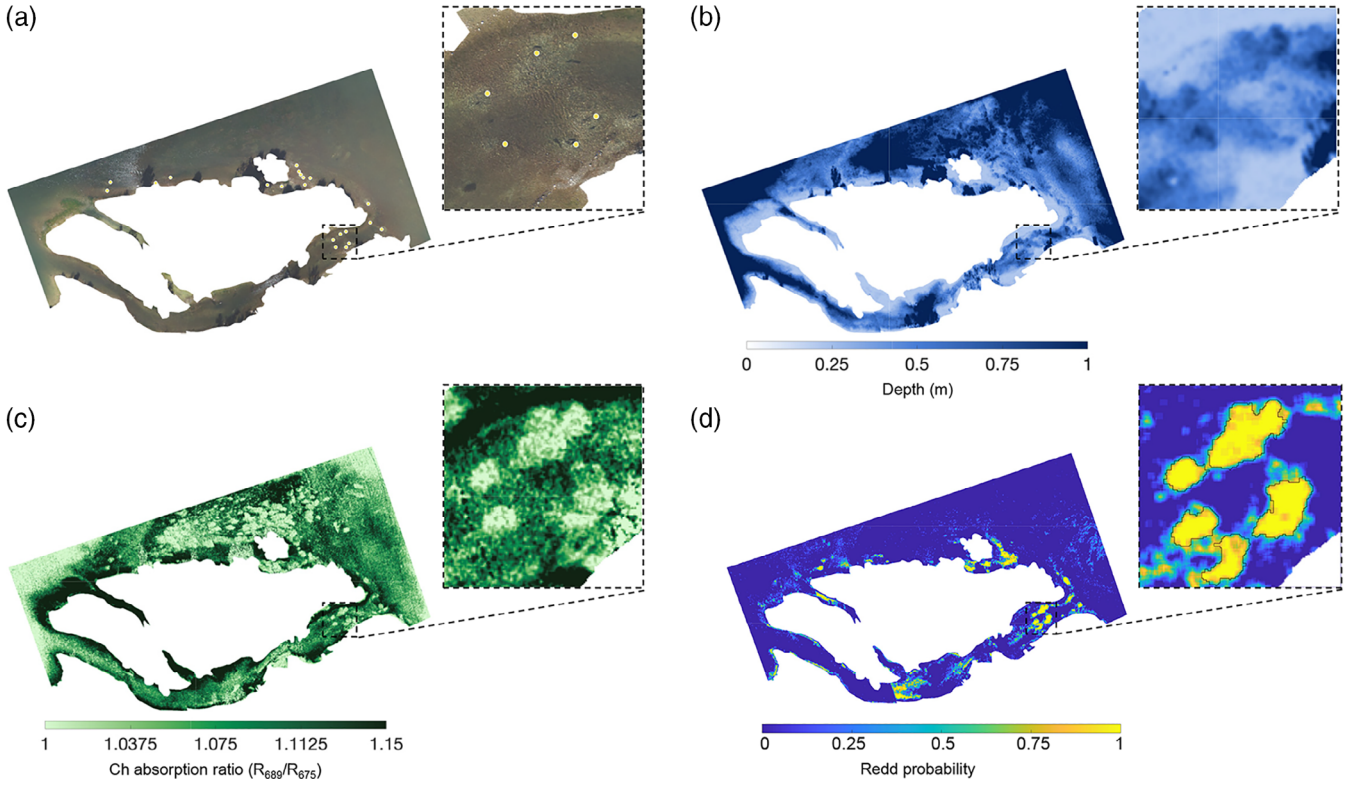

FIGURE 8 UAS-based redd mapping workflow, including (a) imagery with mapped redd locations (b) depth map, (c) *ch* ratio and (d) resulting redd probability map and object-based redd polygons. A scale bar is provided in Figure 1 for reference [Colour figure can be viewed at wileyonlinelibrary.com]

In practice, a number of issues could make spectrally based remote sensing of salmon redds challenging. For example, fall-run Chinook salmon spawn in the American River between November through December at a time when sun angles are low, which might result in shadows along channel margins (Figure 8a). In our study, the effect of shadows was most evident in the depth maps, where the presence of shadows along shallow channel margins led to over-prediction of water depths due to the lower reflectance values typical of deeper water. Because the American River channel was (~100 m) wide, shadows did not significantly affect the overall redd predictions made in this study, but shadows might be more problematic along narrower river channels with dense riparian canopy. The relatively low amount of incident sunlight (i.e., downwelling spectral irradiance) at the time of year when salmon spawn presented another challenge, as lower levels of incident solar energy lead to lower amounts of reflected radiation and thus reduced signal-to-noise ratios in the image data. In our study, we addressed this issue to some degree by flying at a lower height above ground level and decreasing the flight speed of the UAS to allow for a greater image exposure time. While these flight parameters prolonged the duration of the UAS-based image acquisition, the ability to make such adjustments to the flight plan is an important advantage of UAS relative to traditional manned aircraft. UAS allow for greater flexibility in flight planning due to their ability to fly at lower altitudes and use customized flight speeds based on the requirements of a specific project and the environmental conditions at the time of data collection. In addition, UAS deployment also can be more opportunistic than manned aircraft flights, enabling remotely sensed data collection to commence as soon as spawning salmon are observed within the river of interest.

4.2 | Future research

Our work could be extended by integrating other types of remotely sensed data with our redd detection framework to test hypotheses on the physical controls governing salmon redd site selection. While the life-history requirements for spawning salmon have been widely studied, uncertainty persists as to the primary controls on salmon spawning habitat preferences (Lapointe, 2012; Sear, DeVries, & Greig, 2008). For example, water depth preferences of spawning salmon could be quantified by extracting water depths at mapped redd locations from OBRA-based depth maps. Similarly, surface flow velocities derived via particle image velocimetry (PIV) of thermal imagery (Legleiter, Kinzel, & Nelson, 2017) could help to define spawning velocity preferences. UAS-based methods for identifying submerged substrates (Danhoff & Huckins, 2020) and hyporheic exchanges (Pai et al., 2017) also are emerging and could be integrated with our redd mapping approach to further evaluate factors influencing salmon spawning preferences.

Future applications could also use UAS-based, hyperspectral imagery to derive bathymetry and merge this data with topography on dry land to develop continuous digital terrain models (DTMs), similar to prior studies using remote sensing data obtained from manned aircraft (Legleiter, 2012). The DTM could then be used as a boundary condition for developing two-dimensional (2D) flow models to predict water depths and velocities, as done in prior work on a wide, shallow river channel using RGB imagery and SfM techniques (Tamminga et al., 2015). The combination of image-based redd mapping and 2D flow modelling could greatly improve our understanding of the controls on redd site selection by quantifying salmon utilization of natural and restored habitats.

The methods developed in this study provide a means to characterize salmon spawning preferences at intermediate spatial scales (tens of meters to several kilometres), which has been identified as a highly relevant scale for understanding interactions between fish and their environment (Fausch et al., 2002). However, the potential for UAS-based redd mapping has not yet been demonstrated at the larger river segment scale, such as the annual redd census conducted over ~30 km of the lower American River. One of the major hurdles for moving beyond reach-scale redd mapping using UAS in the United States is that the platform must be within visual line of sight of the UAS pilot during operations, due to Federal Aviation Administration (FAA) regulations. Redd sampling over larger spatial extents using UAS platforms could proceed by randomly sampling locations from within a larger river corridor and conducting focused redd mapping at those sites (Groves et al., 2016). Chinook salmon tend to spawn in the same locations each year (Klett, Torgersen, Henning, & Murray, 2013), and thus prior knowledge of existing spawning locations could be used to identify potential UAS study reaches within the river corridor. Redd mapping over longer reaches also could be achieved by deploying the UAS from a series of locations along the river and assembling an image mosaic composed of data from several different flights. For example, a boat could be used to transit between bars from which the UAS could be launched. UAS-based redd mapping potentially could be conducted at broader spatial scales via beyond visible line of sight operations, though these require special FAA waivers.

Until the regulatory process for UAS operations advances, redd mapping using a hybrid approach with aerial imagery obtained from manned aircraft at river segment scales (tens of km) and UAS collected at reach scales could be a promising option. Acquisition of UAS imagery at several sites, collected at the same time as the manned aircraft flights could help improve the redd mapping accuracy over larger spatial extents, where the UAS imagery could provide a means to validate redds mapped from the imagery acquired from manned aircraft. The machine learning classification and object detection approaches used here could also be tested on manned aircraft imagery in an attempt to automate redd detection over larger spatial scales and reduce potential errors made by visual redd mapping from the imagery. Scaling up the redd mapping workflow and integrating UAS imagery with other traditional remote sensing data sets for the purpose of identifying salmon redds remains a priority for future research.

5 | CONCLUSIONS

Our study found that both UAS-based RGB and hyperspectral imagery could be used to identify salmon redds along a large, clear-flowing river, but with varying degrees of accuracy. Salmon redds were visible in the RGB imagery and could be manually counted, similar to traditional visual approaches for redd mapping using photography acquired from manned aircraft. The RGB imagery evaluated in this study was ineffective at mapping complementary habitat information, such as water depth and was less suitable for the machine learning classification approaches tested here. The hyperspectral imagery provided improved accuracy in the overall redd detection and was effective in delineating individual redds via OBIA. Each system had advantages and limitations in terms of the overall accuracy of redd identification and the time required to post-process the data. The RGB sensor required considerably less post-processing time and provided highly accurate spatial positioning, compared to the hyperspectral imagery, suggesting that it might be more suitable for rapid data acquisition or collection of longer time-series imagery data sets. The hyperspectral imagery was able to identify individual redds and effectively map river bathymetry on a large river, therefore providing a potential tool for quantifying both in-stream habitat and the behaviour of spawning salmon. The ability to simultaneously map salmon spawning locations and quantify selected habitat using hyperspectral imagery could facilitate future research aimed at understanding how salmon use and interact with their environment across a range of spatial scales. Such knowledge is key for effective management of salmon populations and for evaluating natural and restored river functionality.

ACKNOWLEDGEMENTS

This investigation was supported by a grant from the NOAA UAS Program Office (Grant # P1610802). We thank Christian Torgersen and an anonymous reviewer for constructive reviews that significantly improved the paper. We also thank Peter Dudley, Jeff Harding, Matt Pickett, JD Richey, Nicholas Wagner, and Jason Woolard for assistance collecting field and UAS data and Mike Aslaksen for overall project support. We would also like to acknowledge Jordan Snyder for providing assistance in post-processing the Nano hyperspectral imagery.

CONFLICT OF INTEREST

The authors declare no conflict of interest. Any use of trade, firm, or product names is for descriptive purposes only and does not imply endorsement by the U.S. Government.

DATA AVAILABILITY STATEMENT

All of the remotely sensed data and field measurements used in this study are available through a data release published by the USGS ScienceBase Catalog (Legleiter and Harrison, 2020).

ORCID

Lee R. Harrison https://orcid.org/0000-0002-5219-9280
Carl J. Legleiter https://orcid.org/0000-0003-0940-8013

Brandon T. Overstreet https://orcid.org/0000-0001-7845-6671
Tom W. Bell https://orcid.org/0000-0002-0173-2866

REFERENCES

Abt, S., Wittier, R., Taylor, A., & Love, D. (1989). Human stability in a high flood hazard zone. *JAWRA Journal of the American Water Resources Association*, *25*, 881–890. https://doi.org/10.1111/j.1752-1688.1989.tb05404.x

Agisoft. (2020). Agisoft metashape. Retrieved from https://www.agisoft.com/

Beakes, M. P., Moore, J. W., Retford, N., Brown, R., Merz, J. E., & Sogard, S. M. (2014). Evaluating statistical approaches to quantifying juvenile Chinook Salmon habitat in a regulated California river. *River Research and Applications*, *30*, 180–191. https://doi.org/10.1002/rra.2632

Beechie, T. J., Sear, D. A., Olden, J. D., Pess, G. R., Buffington, J. M., Moir, H., … Pollock, M. M. (2010). Process-based principles for restoring river ecosystems. *Bioscience*, *60*, 209–222. https://doi.org/10.1525/bio.2010.60.3.7

Benjankar, R., Tonina, D., Marzadri, A., McKean, J., & Isaak, D. J. (2016). Effects of habitat quality and ambient hyporheic flows on salmon spawning site selection. *Journal of Geophysical Research-Biogeosciences*, *121*, 1222–1235. https://doi.org/10.1002/2015JG003079

Bjornn, T., & Reiser, D. (1991). Habitat requirements of salmonids in streams. In W. Meehan (Ed.), *Influences of forest and rangeland management on salmonid fishes and their habitats* (pp. 83–138). Bethesda, MD: American Fisheries Society.

Buters, T. M., Bateman, P. W., Robinson, T., Belton, D., Dixon, K. W., & Cross, A. T. (2019). Methodological ambiguity and inconsistency constrain unmanned aerial vehicles as a silver bullet for monitoring ecological restoration. *Remote Sensing*, *11*, 1180. https://doi.org/10.1002/9781119940791

Carbonneau, P., Fonstad, M. A., Marcus, W. A., & Dugdale, S. J. (2012). Making riverscapes real. *Geomorphology*, *137*, 74–86. https://doi.org/10.1016/j.geomorph.2010.09.030

Danhoff, B. M., & Huckins, C. J. (2020). Modelling submerged fluvial substrates with structure-from-motion photogrammetry. *River Research and Applications*, *36*, 128–137. https://doi.org/10.1002/rra.3532

Dietrich, J. T. (2017). Bathymetric structure-from-motion: Extracting shallow stream bathymetry from multi-view stereo photogrammetry. *Earth Surface Processes and Landforms*, *42*, 355–364. https://doi.org/10.1002/esp.4060

DJI. (2020). Matrice 200 series. Retrieved from https://www.dji.com/matrice-200-series

DroneDeploy. (2020). DroneDeploy flight planning. Retrieved from https://www.dronedeploy.com

Fausch, K. D., Torgersen, C. E., Baxter, C. V., & Li, H. W. (2002). Landscapes to riverscapes: Bridging the gap between research and conservation of stream fishes. *Bioscience*, *52*, 483–498. https://doi.org/10.1641/0006-3568(2002)052[0483:Ltrbtg]2.0.Co;2

Gallagher, S., Hahn, P., & Johnson, D. (2007) Redd counts). In e. D. Johnson (Ed.), *Salmonid field protocols handbook: Techniques for assessing status and trends in Salmon and Trout populations* (pp. 197–234). Bethesda, MD: American Fisheries Society.

Gallagher, S. P., & Gallagher, C. M. (2005). Discrimination of Chinook Salmon, Coho Salmon, and steelhead redds and evaluation of the use of redd data for estimating escapement in several unregulated streams in northern California. *North American Journal of Fisheries Management*, *25*, 284–300. https://doi.org/10.1577/M04-016.1

Geist, D. R., & Dauble, D. D. (1998). Redd site selection and spawning habitat use by fall Chinook Salmon: The importance of geomorphic features in large rivers. *Environmental Management*, *22*, 655–669. https://doi.org/10.1007/s002679900137

Groves, P. A., Alcorn, B., Wiest, M. M., Maselko, J. M., & Connor, W. P. (2016). Testing unmanned aircraft systems for salmon spawning surveys. *Facets*, *1*, 187–204. https://doi.org/10.1139/facets-2016-0019

Hannon, J. (2017). *Annual Chinook Salmon redd counts from aerial photos on the lower American River, California, 2003–2016. United States Bureau of Reclamation*. Sacramento, CA: Bay-Delta Office.

Hanrahan, T. P. (2007). Bedform morphology of salmon spawning areas in a large gravel-bed river. *Geomorphology*, *86*, 529–536. https://doi.org/10.1016/j.geomorph.2006.09.017

Harris, J. M., Nelson, J. A., Rieucau, G., & Broussard, W. P. (2019). Use of drones in fishery science. *Transactions of the American Fisheries Society*, *148*, 687–697. https://doi.org/10.1002/tafs.10168

Harris Geospatial. (2008). ENVI feature extraction module user's guide. Retrieved from https://www.harrisgeospatial.com/docs/rule_based_classification.html

Harrison, L. R., Bray, E., Overstreet, B., Legleiter, C. J., Brown, R. A., Merz, J. E., … Dunne, T. (2019). Physical controls on salmon redd site selection in restored reaches of a regulated, gravel-bed river. *Water Resources Research*, *55*, 8942–8966. https://doi.org/10.1029/2018wr024428

Headwall Photonics. (2020a). Nano-hyperspec. Retrieved from http://www.headwallphotonics.com/spectral-imaging/hyperspectral/nano-hyperspec

Headwall Photonics. (2020b) Spectralview. Retrieved from https://www.headwallphotonics.com/software

Hugue, F., Lapointe, M., Eaton, B. C., & Lepoutre, A. (2016). Satellite-based remote sensing of running water habitats at large riverscape scales: Tools to analyze habitat heterogeneity for river ecosystem management. *Geomorphology*, *253*, 353–369. https://doi.org/10.1016/j.geomorph.2015.10.025

Isaak, D. J., & Thurow, R. F. (2006). Network-scale spatial and temporal variation in Chinook Salmon *(Oncorhynchus tshawytscha)* redd distributions: Patterns inferred from spatially continuous replicate surveys. *Canadian Journal of Fisheries and Aquatic Sciences*, *63*, 285–296. https://doi.org/10.1139/f05-214

Klett, K. J. C., Torgersen, C. E., Henning, J. A., & Murray, C. J. (2013). Spatial consistency of Chinook salmon redd distribution within and among years in the cowlitz river, Washington. *North American Journal of Fisheries Management*, *33*, 508–518. https://doi.org/10.1080/02755947.2013.778924

Lapointe, M. (2012). River geomorphology and salmonid habitat: Some examples illustrating their complex association, from redd to riverscape scales. In M. Church, P. M. Biron, & A. G. Roy (Eds.), *Gravel-bed rivers: Processes, tools, environments* (pp. 191–215). Chichester, UK: John Wiley.

Legleiter, C. J. (2012). Remote measurement of river morphology via fusion of LiDAR topography and spectrally based bathymetry. *Earth Surface Processes and Landforms*, *37*, 499–518. https://doi.org/10.1002/esp.2262

Legleiter, C. J., & Harrison, L. R. (2019). Remote sensing of river bathymetry: Evaluating a range of sensors, platforms, and algorithms on the upper Sacramento River, California, USA. *Water Resources Research*, *55*, 2142–2169. https://doi.org/10.1029/2018wr023586

Legleiter, C. J., & Harrison, L. R. (2020). Image data and field measurements used to map salmon spawning locations via remote sensing, American River, California, November 5–7, 2018. *U.S. Geological Survey data release*. https://doi.org/10.5066/P998CGA2

Legleiter, C. J., Kinzel, P. J., & Nelson, J. M. (2017). Remote measurement of river discharge using thermal particle image velocimetry (PIV) and various sources of bathymetric information. *Journal of Hydrology*, *554*, 490–506. https://doi.org/10.1016/j.jhydrol.2017.09.004

Legleiter, C. J., & Overstreet, B. T. (2012). Mapping gravel bed river bathymetry from space. *Journal of Geophysical Research-Earth Surface*, *117*, F04024. https://doi.org/10.1029/2012jf002539

Legleiter, C. J., & Overstreet, B. T. (2014). Retrieving river attributes from remotely sensed data: An experimental evaluation based on field spectroscopy at the outdoor stream lab. *River Research and Applications*, *30*, 671–684. https://doi.org/10.1002/rra.2674

Legleiter, C. J., Roberts, D. A., & Lawrence, R. L. (2009). Spectrally based remote sensing of river bathymetry. *Earth Surface Processes and Landforms*, *34*, 1039–1059. https://doi.org/10.1002/esp.1787

Malcolm, I. A., Gibbins, C. N., Soulsby, C., Tetzlaff, D., & Moir, H. J. (2012). The influence of hydrology and hydraulics on salmonids between spawning and emergence: Implications for the management of flows in regulated rivers. *Fisheries Management and Ecology*, *19*, 464–474. https://doi.org/10.1111/j.1365-2400.2011.00836.x

Moir, H. J., & Pasternack, G. B. (2008). Relationships between mesoscale morphological units, stream hydraulics and Chinook Salmon *(Oncorhynchus tshawytscha)* spawning habitat on the lower Yuba River, California. *Geomorphology*, *100*, 527–548. https://doi.org/10.1016/j.geomorph.2008.02.001

Moir, H. J., & Pasternack, G. B. (2010). Substrate requirements of spawning Chinook Salmon *(Oncorhynchus tshawytscha)* are dependent on local channel hydraulics. *River Research and Applications*, *26*, 456–468. https://doi.org/10.1002/rra.1292

Moyle, P., Lusardi, R., Samuel, P., & Katz, J. (2017). *State of the Salmonids: Status of California's emblematic fishes 2017*. San Francisco, CA: University of California, Davis and California Trout.

Pai, H., Malenda, H. F., Briggs, M. A., Singha, K., Gonzalez-Pinzon, R., Gooseff, M. N., … Team, A. (2017). Potential for small unmanned aircraft systems applications for identifying groundwater-surface water exchange in a meandering river reach. *Geophysical Research Letters*, *44*, 11868–11877. https://doi.org/10.1002/2017gl075836

Piegay, H., Arnaud, F., Belletti, B., Bertrand, M., Bizzi, S., Carbonneau, P., … Slater, L. (2020). Remotely sensed rivers in the anthropocene: State of the art and prospects. *Earth Surface Processes and Landforms*, *45*, 157–188. https://doi.org/10.1002/esp.4787

Riebe, C. S., Sklar, L. S., Overstreet, B. T., & Wooster, J. K. (2014). Optimal reproduction in salmon spawning substrates linked to grain size and fish length. *Water Resources Research*, *50*, 898–918. https://doi.org/10.1002/2013wr014231

Roncoroni, M., & Lane, S. N. (2019). A framework for using small unmanned aircraft systems (sUASs) and SfM photogrammetry to detect salmonid redds. *Ecological Informatics*, *53*, 100976. https://doi.org/10.1016/j.ecoinf.2019.100976

Sear, D. A., DeVries, P., & Greig, S. M. (2008). The science and practice of salmonid spawning habitat remediation. In D. Sear & P. DeVries (Eds.), *Salmonid Spawning Habitat in Rivers: Physical Controls, Biological Responses, and Approaches to Remediation* (Vol. 65, pp. 1–13). Bethesda, MD: American Fisheries Society Press.

Tamminga, A., Hugenholtz, C., Eaton, B., & Lapointe, M. (2015). Hyperspatial remote sensing of channel reach morphology and hydraulic fish habitat using an unmanned aerial vehicle (Uav): A first assessment in the context of river research and management. *River Research and Applications*, *31*, 379–391. https://doi.org/10.1002/rra.2743

Tomsett, C., & Leyland, J. (2019). Remote sensing of river corridors: A review of current trends and future directions. *River Research and Applications*, *35*, 779–803. https://doi.org/10.1002/rra.3479

UgCS. (2020). Universal ground control software (UgCS). Retrieved from https://www.ugcs.com

Visser, R., Dauble, D. D., & Geist, D. R. (2002). Use of aerial photography to monitor fall Chinook Salmon spawning in the Columbia River. *Transactions of the American Fisheries Society*, *131*, 1173–1179. https://doi.org/10.1577/1548-8659(2002)131<1173:Uoaptm>2.0.Co;2

Woodget, A. S., Visser, F., Maddock, I. P., & Carbonneau, P. E. (2016). The accuracy and reliability of traditional surface flow type mapping: Is it time for a new method of characterizing physical river habitat? *River Research and Applications*, *32*, 1902–1914. https://doi.org/10.1002/rra.3047

Yoshiyama, R. M., Gerstung, E. R., Fisher, F. W., & Moyle, P. B. (2001). Historical and present distribution of Chinook Salmon in the Central Valley drainage of California. In R. Brown (Ed.), *Fish Bulletin 179: Contributions to the biology of Central Valley salmonids* (Vol. 1, pp. 71–176). Sacramento, CA: California Department of Fish and Game.

Zeug, S. C., Sellheim, K., Watry, C., Rook, B., Hannon, J., Zimmerman, J., … Merz, J. (2014). Gravel augmentation increases spawning utilization by anadromous salmonids: A case study from California, USA. *River Research and Applications*, *30*, 707–718. https://doi.org/10.1002/rra.2680

How to cite this article: Harrison LR, Legleiter CJ, Overstreet BT, Bell TW, Hannon J. Assessing the potential for spectrally based remote sensing of salmon spawning locations. *River Res Applic*. 2020;36:1618–1632. https://doi.org/10.1002/rra.3690